



RESEARCH ARTICLE

10.1002/2016JD025753

Generation of real-time mode high-resolution water vapor fields from GPS observations

Chen Yu¹ , Nigel T. Penna¹ , and Zhenhong Li¹ ¹School of Civil Engineering and Geosciences, Newcastle University, Newcastle upon Tyne, UK

Key Points:

- An iterative tropospheric decomposition model for zero differenced ZTD interpolation
- Generation of high-resolution real-time mode GPS-based ZTD and PWV maps
- Validation of ITD PWV maps with the MODIS near-IR water vapor product

Correspondence to:

Z. Li,
Zhenhong.Li@newcastle.ac.uk

Citation:

Yu, C., N. T. Penna, and Z. Li (2017), Generation of real-time mode high-resolution water vapor fields from GPS observations, *J. Geophys. Res. Atmos.*, 122, 2008–2025, doi:10.1002/2016JD025753.

Received 5 AUG 2016

Accepted 22 JAN 2017

Accepted article online 26 JAN 2017

Published online 11 FEB 2017

Abstract Pointwise GPS measurements of tropospheric zenith total delay can be interpolated to provide high-resolution water vapor maps which may be used for correcting synthetic aperture radar images, for numeral weather prediction, and for correcting Network Real-time Kinematic GPS observations. Several previous studies have addressed the importance of the elevation dependency of water vapor, but it is often a challenge to separate elevation-dependent tropospheric delays from turbulent components. In this paper, we present an iterative tropospheric decomposition interpolation model that decouples the elevation and turbulent tropospheric delay components. For a 150 km × 150 km California study region, we estimate real-time mode zenith total delays at 41 GPS stations over 1 year by using the precise point positioning technique and demonstrate that the decoupled interpolation model generates improved high-resolution tropospheric delay maps compared with previous tropospheric turbulence- and elevation-dependent models. Cross validation of the GPS zenith total delays yields an RMS error of 4.6 mm with the decoupled interpolation model, compared with 8.4 mm with the previous model. On converting the GPS zenith wet delays to precipitable water vapor and interpolating to 1 km grid cells across the region, validations with the Moderate Resolution Imaging Spectroradiometer near-IR water vapor product show 1.7 mm RMS differences by using the decoupled model, compared with 2.0 mm for the previous interpolation model. Such results are obtained without differencing the tropospheric delays or water vapor estimates in time or space, while the errors are similar over flat and mountainous terrains, as well as for both inland and coastal areas.

1. Introduction

Time-varying two-dimensional precipitable water vapor (PWV) fields (maps) are used in meteorological now-casting, including the identification of events dominated by horizontal advection [Benevides *et al.*, 2015], for assessing moisture transport in the lower troposphere [e.g., Mengistu Tsidu *et al.*, 2015], for relating humidity fields to precipitation events [e.g., Boniface *et al.*, 2009], for assessing the severity of tropical cyclones [e.g., Shoji *et al.*, 2011], and for assessing the impact of new assimilated observations for forecasting precipitation [e.g., Yan *et al.*, 2009]. Such maps are also essential for correcting synthetic aperture radar (SAR) images for atmospheric effects to enable small (and long wavelength) geophysical signals to be measured, including interseismic strain accumulation and postseismic motion, observations of which not only give insight into the mechanics of a fault but also play key roles in estimating the likelihood of future earthquakes [Wright *et al.*, 2004; Gourmelen and Amelung, 2005; Fialko, 2006; Walters *et al.*, 2013; Wen *et al.*, 2012; Li *et al.*, 2009a]. Dense PWV fields also enable Global Navigation Satellite Systems (GNSS) Network Real-time Kinematic (RTK) observations to be corrected for signal delays due to water vapor on propagating from space through the Earth's neutral atmosphere ("troposphere") to a ground-based receiver. Such corrections are essential for centimeter-level positioning, particularly heights, and enable (subject to sufficient GNSS base station coverage) Network RTK to be used for geophysical and engineering applications that have normally only used local base station RTK, such as river channel mapping [e.g., Brasington *et al.*, 2003], glacier flow and debris mapping [e.g., De Paoli and Flowers, 2009], coastal erosion [e.g., Lee *et al.*, 2013], crustal deformation [e.g., Genrich and Bock, 2006] and structural [e.g., Im *et al.*, 2013] monitoring, precision farming [e.g., Pérez-Ruiz *et al.*, 2011], embankment instability, and landslide monitoring [e.g., Gili *et al.*, 2000; Zabuski *et al.*, 2015].

Two-dimensional PWV maps/fields may be obtained directly from the National Aeronautics and Space Administration (NASA) Moderate Resolution Imaging Spectroradiometer (MODIS) on board each of the Terra and Aqua satellites (launched in 1999 and 2002, respectively). They provide global coverage every 1–2 days with observations in 36 spectral bands at moderate resolution (250–1000 m), five of which (near-infrared (IR)) are used for remote sensing of water vapor with 1 km spatial resolution over clear land areas,

©2017. The Authors.

This is an open access article under the terms of the Creative Commons Attribution License, which permits use, distribution and reproduction in any medium, provided the original work is properly cited.

oceanic areas with Sun glint, and/or above clouds over both land and ocean [Gao and Kaufman, 2003]. MODIS swaths do not coincide in time with images from SAR satellites such as ERS-1/2 (nominally 30 min of time difference), Envisat (nominally 30 min of time difference), or Sentinel-1 (nominally 4.5 h of time difference); therefore, for SAR atmospheric corrections, temporal interpolation errors will always prevail. The Envisat SAR satellite included the Medium-Resolution Imaging Spectrometer (MERIS), a passive push-broom imaging instrument measuring the solar radiation reflected from the Earth's surface and clouds in the visible and near-IR spectral range during the daytime. MERIS provided near-IR water vapor products above land or ocean surfaces under cloud-free conditions [Bennartz and Fischer, 2001] or above the highest cloud level under cloudy conditions [Albert et al., 2001] at two nominal spatial resolutions: 0.3 km for full-resolution mode and 1.2 km for reduced-resolution mode. Both MODIS and MERIS near-IR PWV measurements have been validated against radiosonde and GPS-based products at discrete points with 1 mm and 1.2 mm respective RMS agreements [Li et al., 2009b; Li et al., 2006b; Li et al., 2005; Li et al., 2003; Li et al., 2006c]. However, neither the MODIS nor MERIS instruments provide reliable PWV values above land or ocean surfaces when clouds are present, which restricts their use. Similarly, the Atmospheric Infrared Sounder (AIRS) instrument, also on board the Aqua satellite, not only provides global coverage amounting to 324,000 PWV profiles with a vertical resolution of 2 km and a spatial resolution at nadir of 45 km but also only operates in clear skies and in partly cloudy conditions [Aumann et al., 2003]. Comparisons between AIRS products and GPS PWV showed RMS differences of about 3–4 mm and 15% differences in the 2 km layers between AIRS and radiosondes [Divakarla et al., 2006; Raja et al., 2008]. PWV fields may also be obtained from global atmospheric models (both reanalysis and rapid update cycle predictions) but suffer from their coarse spacing, low temporal resolution (e.g., 3 or 6 h for the European Centre for Medium-Range Weather Forecasts (ECMWF) model), and failures during periods of atmospheric turbulence [Jolivet et al., 2014].

GPS provides a means of obtaining PWV with continuous temporal resolution without any cloud or weather dependence, albeit at discrete points where the GPS receivers are located. First, the time-varying tropospheric zenith total delay (ZTD) is estimated per receiver by using the GPS data alone, and then the zenith hydrostatic "dry" delay (which may be accurately modeled by using surface pressure data) is subtracted to leave the zenith wet delay (ZWD), which is spatially and temporally much more variable. The ZWD may then be readily converted to PWV by using estimates of the mean temperature of the atmosphere, based on surface temperature measurements [Bevis et al., 1992]. The pointwise GPS PWV measurements agree to those from radiosondes and microwave radiometers with standard deviations of about 1–2 mm [e.g., Ohtani and Naito, 2000; Liou et al., 2001; Li et al., 2003] and may then be interpolated to provide PWV fields, which has been attempted by using different models. For example, Jarlemark and Emardson [1998] evaluated a gradient model, a linear regression in time model that ignored observational directions, and a turbulence model that yielded at least 10% improved RMS error than the other two models. Williams et al. [1998] used a structure function to model the water vapor variation in space, but with respect to a reference value, while Janssen et al. [2004] not only found that Inverse Distance Weighted (IDW) and Ordinary Kriging interpolation models perform better than spline interpolation but also only considered double-differenced ZTDs as they were considering interferometric synthetic aperture radar (InSAR) atmospheric corrections only. A deficiency of all these models is that they did not consider the terrain elevation dependence of water vapor, and hence, the interpolated values may contain large errors in regions with highly varying topography [e.g., Walters et al., 2013]. To deal with the water vapor stratification, Emardson and Johansson [1998] incorporated a height scaling function with a best linear unbiased estimator and suggested an interpolated ZWD accuracy of about 1 cm, but only one station in Sweden was considered and the height variation across the network was only about 200 m. Li et al. [2006a] proposed a GPS topography-dependent turbulence model but reported that interpolation models should be applied to ZTD/ZWD values differenced in time rather than the absolute ZTD/ZWD values themselves, as this can reduce the influence of topographic effects on the ZTD/ZWD variations. For interpolating undifferenced GPS ZWD point values, Onn and Zebker [2006] utilized a frozen flow hypothesis to model the water vapor variation in time. Then Xu et al. [2011] showed that incorporating this height scaling function approach with an interpolator model based on the estimator of simple Kriging with varying local means (we will refer to this model as SKlm + Onn) improved the ZWD interpolation RMS accuracy by 29% compared with using the Berrada Baby et al. [1988] semiempirical height scaling function. In a different approach to account for variations with topography, Bekaert et al. [2015] employed an InSAR phase observation-based power law correction model which used a fixed reference at the relative top of the

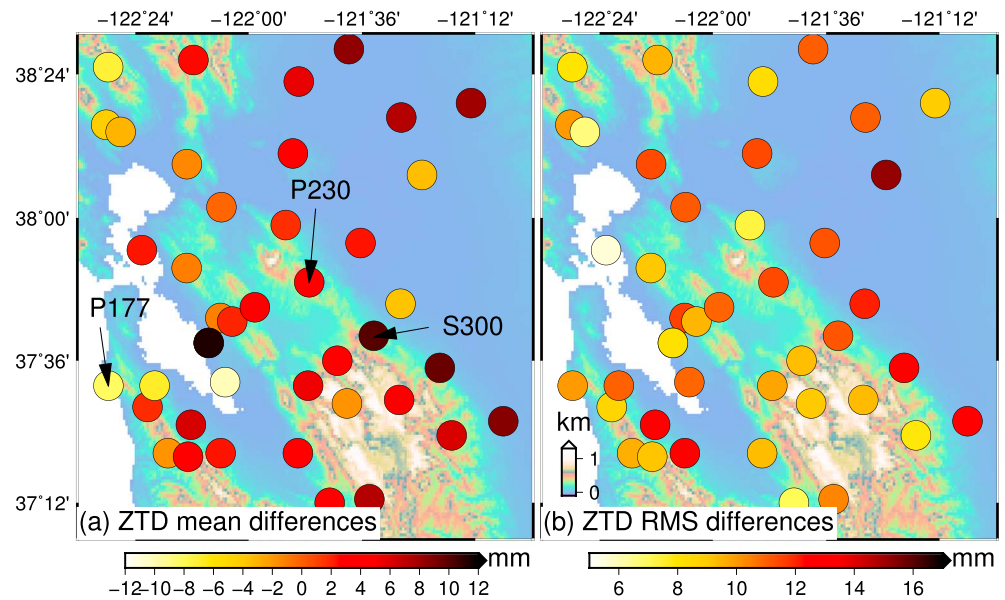


Figure 1. (a) Mean and (b) RMS differences per station between RTPPP and GIPSY ZTDs, estimated every 5 min on 2 September 2015 for all 41 GPS stations in the California study region. For all stations, the mean difference and the mean RMS difference are 1.9 mm and 10.1 mm, respectively, with this day being indicative of the median differences for all days of 2015. The white area represents the Pacific Ocean and San Francisco Bay, and the background shows the elevation. Stations P177, P230, and S300 are labeled as they are considered in Figure 9.

troposphere and described how the phase delay varies with altitude. To separate deformation and tropospheric signals, a frequency band insensitive to deformation is required. *Benevides et al.* [2016] also attempted to constrain GPS PWV with InSAR-derived PWV maps containing the topography signal. However, these models did not take into account that the InSAR measurements themselves have uncertainties of up to several centimeters and are susceptible to not detecting geophysical signals such as volcano inflation/deflation and interseismic slip rate [*Williams et al.*, 1998]. Hence, we consider the SKIm + Onn model to represent the current state of the art for the generation of PWV maps.

Several previous studies have noticed the coupling effect of the tropospheric turbulence and terrain elevation dependency [e.g., *Treuhaft and Lanyi*, 1987; *Li et al.*, 2006a; *Xu et al.*, 2011; *Benevides et al.*, 2016]. However, in the presence of strong atmospheric turbulence, previous models are inadequate for correcting SAR images to be used for subcentimeter-level ground motion monitoring [e.g., *Walters et al.*, 2013; *Fattahi and Amelung*, 2015] or for the highest Network RTK positional precisions when such variations are not eliminated by data differencing. The aim of this study is therefore to improve the accuracy of GPS interpolated tropospheric water vapor maps by accounting for the coupling effect of both the terrain elevation dependency and tropospheric turbulence, demonstrate this over varying terrain, and compare with the SKIm + Onn model. We generate temporally continuous high spatial resolution maps by using undifferenced (neither spatially nor temporally) ZTD values estimated pointwise at GPS stations by using the precise point positioning processing (PPP) technique in real-time mode. Hence, they are directly applicable for correcting SAR images, enabling rapid response to ground motion from large earthquakes and volcanoes, for removing tropospheric effects in Network RTK GPS processing, and for meteorological nowcasting via potential assimilation in numerical weather models, noting that ZTD is the form of GPS-based water vapor observation used operationally by, for example, the Met Office [*Bennett and Jupp*, 2012] and Météo-France [*Poli et al.*, 2007]. We validate our interpolated absolute ZTD fields first by cross validation with the GPS pointwise ZTDs, and then by converting to PWV and comparing with the MODIS near-IR water vapor product, which we choose due to its high spatial resolution and accuracy [*Li et al.*, 2003]. The MERIS near-IR water vapor product has similar quality with an even higher spatial resolution [*Li et al.*, 2006c], but it is only available during the period from May 2002 and April 2012 before the International GNSS Real-time Service began (April 2013). We use data from all of 2015 (hence covering all four seasons) for a study region of California of about 150 km × 150 km, i.e., 37°06' to 38°30'N and 122°40' to 121°00'W, incorporating 41 Plate Boundary Observatory (PBO) GPS

stations, as shown in Figure 1. This region was selected as there is a dense spacing of continuous GPS stations whose data have been extensively analyzed previously (including postprocessed ZTDs readily available for quality control), it is comparable to the size of a SAR image swath (e.g., 100 km for Envisat stripmap mode and 250 km for Sentinel-1 Interferometric Wide Swath mode), there are large variations in topography, and it experiences relatively cloud-free conditions as needed for validation with MODIS.

2. Iterative Tropospheric Decomposition Model

Tropospheric delays, especially the part due to atmospheric water vapor, vary both vertically and laterally over short distances and are often considered as the sum of (i) a stratified component highly correlated with topography which therefore delineates the vertical tropospheric profile and (ii) a turbulent component resulting from disturbance processes (e.g., severe weather) in the troposphere which trigger uncertain patterns in space and time [Williams et al., 1998; Cho et al., 2003; Li et al., 2006a]. We present an iterative tropospheric decomposition (ITD) model to effectively separate the turbulent- and elevation-dependent ZTD components. The ITD model decouples the ZTD into stratified and turbulent delays, which enable the more accurate interpolation of dense ZTD fields from pointwise values from a set of GPS reference stations across a region. It is defined as

$$\text{ZTD}_k = T(\mathbf{x}_k) + L_0 e^{-\beta \bar{h}_k} + \varepsilon_k \quad (1)$$

where, for the ZTD at location k , T represents the turbulent component and \mathbf{x}_k is the station coordinate vector in the local topocentric coordinate system; the stratified component is represented with an exponential function with coefficient β in which L_0 is, for the region considered, the stratified component delay at sea level and $\bar{h}_k = (h_k - h_{\min}) / (h_{\max} - h_{\min})$ is the scaled height; ε_k represents the remaining unmodeled residual errors, including unmodeled stratified and turbulent signals. The turbulent component usually consists of medium-to-long wavelength signals that can be interpolated by an IDW method. If n GPS stations are used in the region considered, then the IDW model reads as

$$T_u = \sum_{i=1}^n w_{ui} T(\mathbf{x}_i) \quad \text{and} \quad w_{ui} = \frac{d_{ui}^{-2}}{\sum_{i=1}^n d_{ui}^{-2}} \quad (2)$$

where w_{ui} denotes the interpolation coefficient; u and i are indices for the user and reference stations, respectively; and d_{ui} represents the horizontal distance from the user to reference station. Reference stations at distances more than 100 km from the user station show limited correlation [Emardson and Johansson, 1998], so they are not used.

In order to decompose the ZTD into stratified and turbulent components, which can account for substantial amounts of the ZTD but behave very differently, an iterative separation procedure was used:

1. The ZTDs from all GPS stations within the user to reference station decorrelated range limit are used to estimate initial values for the exponential coefficients β and L_0 , assuming that the turbulent component values in equation (1) are zero.
2. The residuals ε_k , which are the summation of the unmodeled errors and the turbulent component, are computed by subtracting per station the stratified delay (as modeled by the estimated exponential coefficients) from the ZTD.
3. The turbulent component, T in equation (1), is computed per reference station from the residuals ε_k by using the IDW function w_{ui} given in equation (2):

$$\begin{bmatrix} T_1 \\ T_2 \\ \dots \\ T_n \end{bmatrix} = \begin{bmatrix} 0 & w_{12} & \dots & w_{1n} \\ w_{21} & 0 & \dots & w_{2n} \\ \dots & \dots & 0 & \dots \\ w_{n1} & \dots & w_{n,n-1} & 0 \end{bmatrix} \begin{bmatrix} \varepsilon_1 \\ \varepsilon_2 \\ \dots \\ \varepsilon_n \end{bmatrix} \quad (3)$$

4. The updated values for the turbulent component per reference station are subtracted from the ZTD per reference station in equation (1), and a new set of exponential coefficients are obtained.

5. Steps 2–4 are repeated until the exponential coefficients β and L_0 converge. The final outputs are the exponential coefficients for the decorrelated range limit considered, plus the turbulent delay component and residuals per reference station.
6. The ZTD at the location of interest is obtained by interpolation of the reference station turbulent component and residuals and added to the stratified delay computed by using the final values of the exponential coefficients.

It should be noted that the assumption of the ITD model is that the turbulent component obeys the IDW interpolation law and the stratified component obeys the exponential law and, importantly, that these two components are not tightly coupled together. We later show (section 6 and Figure 9) that the two components are indeed separable and the convergence state can be reached rapidly. Although here we present the ITD model by ZTDs in zero difference mode, it is also suitable for interpolating differenced ZTD or PWV/ZWD. Hence, the input to the ITD model may be, as well as GPS ZTDs, other water vapor products such as those from the ECMWF numerical weather model, MODIS, or their combination.

3. Real-Time Mode GPS ZTD Estimation and Validation

3.1. Real-Time Mode GPS Precise Point Positioning Method

The pointwise ZTD values for the 41 study region GPS stations used for the generation of the interpolated maps were estimated by using real-time mode GPS PPP processing. We used a PPP software which is a highly self-modified version of RTKLIB (www.rtklib.com), employing an extended Kalman filter [Gelb, 1974] to estimate in the state vector the constant ambiguities and time-varying receiver coordinates, receiver and satellite clocks (considered as white noise), while the ZWD was estimated as a random walk parameter as a correction to an a priori ZTD from the UNB3 global empirical model [Leandro et al., 2006], employing the Global Mapping Function [Boehm et al., 2006a], and east-west and north-south tropospheric gradients were estimated. We used the ionospheric free pseudorange and carrier phase observables and applied absolute International GNSS Service (IGS) satellite and receiver antenna phase center offset corrections. We also applied corrections for antenna phase wind up [Beyerle, 2009], relativistic effects [Kouba, 2009], pseudorange differential calibration delays [Kouba, 2009], Earth tide [McCarthy, 1996], and ocean tide loading effects by using FES2004 coefficients obtained from <http://holt.oso.chalmers.se/loading>. Uncalibrated phase and pseudorange hardware delays were assumed to be absorbed by the (float) ambiguity parameters and estimated receiver clocks, respectively.

PPP relies on highly accurate satellite orbits and clocks [Zumberge et al., 1997], which are usually held fixed in postprocessed PPP. For our real-time mode processing, we used fixed satellite orbits from the International GNSS Service (IGS) Real-time Service, which were generated by decoding the IGC01 solution streams (products.igs-ip.net), every 15 s to match the GPS observation sampling rate of the PBO stations used. However, the satellite clocks have unpredictable behavior which makes their real-time prediction challenging [Li et al., 2014], so we did not fix these to the real-time product values but estimated corrections to them by using satellite clock parameters with the Gundlich and Koch [2002] robust estimation method. Additional constraints were introduced to overcome the rank deficiency of the normal equations, namely

$$dt_k - dt_{k,RTS} = 0 \tag{4}$$

$$res(dt_k) = dt_k - dt_{k,RTS} \tag{5}$$

where $dt_{k,RTS}$ is the initial value of the satellite clock given by the real-time product and acts as a pseudo-observation; $res(dt_k)$ and dt_k are the satellite clock residual and value, respectively. The satellite clock parameters were estimated as white noise parameters with a sigma of 0.001 ns, and the error messages contained in the real-time satellite clock product were used to determine the weights of the pseudo-observations in equation (4). An iterative process was used to identify some clock outliers which were hence ignored or assigned less weight in subsequent iterations [Gundlich and Koch, 2002].

We processed the data from 1 January to 31 December 2015 per GPS station in daily, discrete 24 h batches in real-time mode, with an elevation angle cutoff of 10°. The tropospheric delay was estimated every 5 min by using a process noise of $5.0e - 8 \text{ km}/\sqrt{5}$. To enable the fastest PPP solution convergence and separation of the ambiguities from the other estimated parameters, which is particularly problematic when using

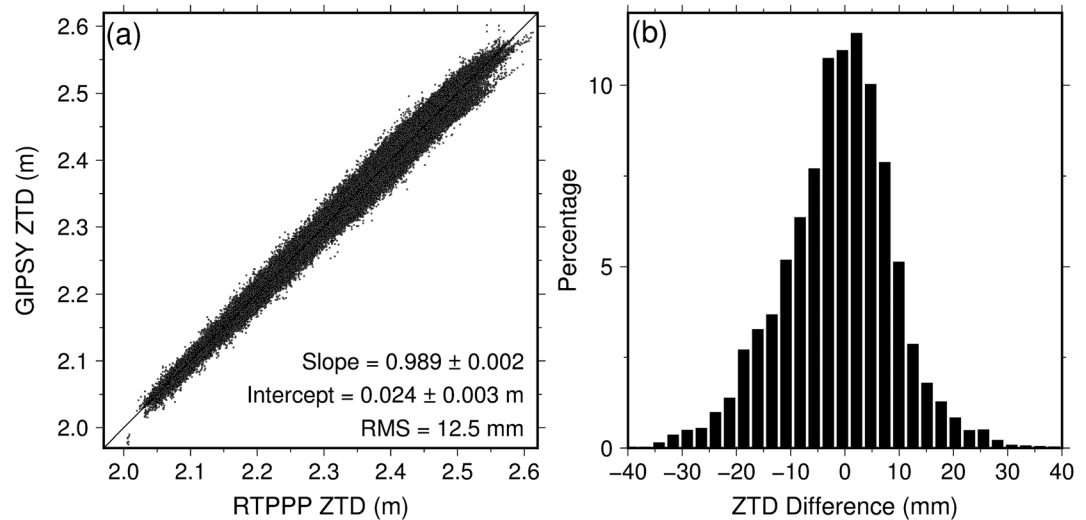


Figure 2. Comparison between RTPPP and GIPSY ZTDs for all 41 GPS reference stations in the California study region, from 1 January to 31 December 2015 at an interval of 5 min. (a) Correlation analysis with a linear model $GIPSY\ ZTD = Slope \times RTPPP\ ZTD + Intercept$ and (b) histogram of the differences.

real-time satellite orbits and clocks [e.g., Yao *et al.*, 2014], we applied loose constraints to a priori receiver coordinate values obtained from the PBO GPS Station Position Time Series (<http://pbo.unavco.org/data/gps>). Nearly 70% of daily solutions converged within 30 min (convergence time here means from the beginning epoch to an epoch whose horizontal component bias is less than 10 cm and height component bias is less than 15 cm, and the overall standard deviation of its next 20 consecutive epochs also satisfies this requirement), with 90% of daily solutions converging within 50 min. The results presented hereafter are based only on the ZTD values after convergence was attained, according to these criteria.

3.2. Validation of Real-Time Mode GPS Pointwise ZTDs

To validate our real-time mode PPP (RTPPP) GPS ZTD estimates per station, we compared with postprocessed 5 min “truth” values computed by the Geodesy Laboratory at Central Washington University by using the NASA Jet Propulsion Laboratory/Caltech GPS Inferred Positioning System (GIPSY) software version 6.2 in PPP mode with fixed IGS final orbits and clocks. The values were obtained from <ftp://data-out.unavco.org/pub/products/troposphere/>, and in their processing, the VMF1 gridded tropospheric mapping function was used together with ECMWF gridded a priori ZHDs and ZWDs [Boehm *et al.*, 2006b], while estimating the ZWD and tropospheric gradients (east-west and north-south) with process noise values of $5.0e - 8\ km/\sqrt{s}$ and $5.0e - 9\ km/\sqrt{s}$, respectively. We computed the differences between our RTPPP and GIPSY ZTDs at the common 5 min epochs, excluded all the outliers greater than three times the standard deviation, then for each station computed per day the mean difference and the root-mean-square (RMS) of the differences to assess the quality of the real-time mode processing. These are shown for a sample day (2 September 2015) in Figure 1, chosen as it is indicative of the median differences for all days of 2015. The mean of the per station differences across the whole network is 1.9 mm for the sample day, indicating that no significant systematic error exists between the RTPPP and GIPSY ZTDs, including stations in mountainous areas. The mean RMS is 10.1 mm, and more than 80% of the stations have an RMS value smaller than 12 mm, which is deemed sufficient quality for assimilation into real-time meteorological models [Shoji *et al.*, 2011].

Apart from considering the spatial distribution of the differences, it is also important to assess the RTPPP performance over time. We therefore in Figure 2 show the 5 min RTPPP ZTDs plotted against the common epoch 5 min GIPSY ZTDs, from all 41 stations for the entire year, and plot the differences as a histogram. A linear regression fit gave $GIPSY\ ZTD = 0.989(\pm 0.002) \times RTPPP\ ZTD + 0.024(\pm 0.003)$, and the correlation coefficient between them was 0.99, demonstrating high consistency between the RTPPP and GIPSY ZTDs not just spatially but also temporally. About 82% of solutions show differences smaller than 15 mm with 73% below 12 mm. The RMS difference is 12.5 mm, commensurate with the spatial RMS difference and further indicating

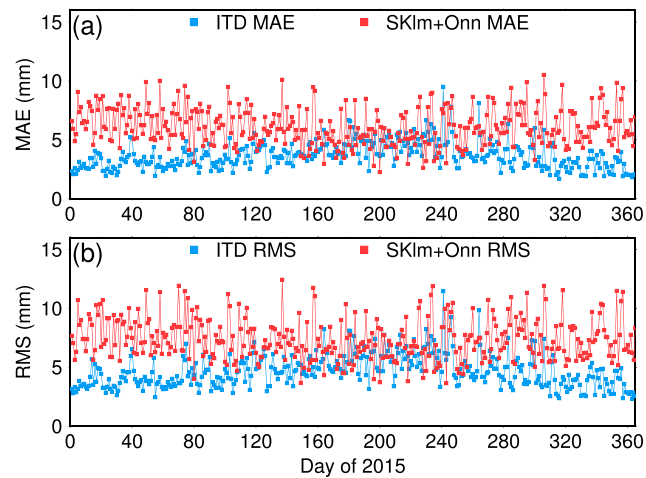


Figure 3. Time series of cross-validated daily MAE and RMS differences, based on 14:00 Pacific standard time (i.e., local time) RTPPP interpolation at all 41 GPS stations using the ITD and SKIm + Onn models and comparing with RTPPP ZTDs. The annual mean MAE values are 3.2 mm for ITD and 6.2 mm for SKIm + Onn, while the annual mean RMS differences are 4.1 mm for ITD and 7.4 mm for SKIm + Onn.

an RTPPP ZTD precision of about 1 cm, which is commensurate with previous real-time studies [e.g., *Li et al., 2014; Ahmed et al., 2016*].

4. Cross Validation of Interpolated ZTD at GPS Stations

Cross validation was used to evaluate the performance of the ITD model for interpolating ZTDs and compared with the SKIm + Onn model. While *Xu et al. [2011]* applied the SKIm + Onn model to ZWD, as ZWD also dominates the spatiotemporal variations of ZTD (with the ZHD being readily determined with surface pressure), we may also apply it to ZTD interpolation. Since the dry and wet components are both important for some applications such as InSAR atmospheric corrections [*Elliott et al., 2008; Jolivet et al., 2014*], and the separation of ZWD from GPS-derived ZTD will introduce additional uncertainties, it is better to use total delays rather than wet delays only. To provide an indication of the ZTD quality used for single-epoch SAR corrections, and to be commensurate with subsequent MODIS validations (section 5), we adopted the approach of *Xu et al. [2011]* and used one ZTD value per day (that at 14:00 Pacific standard time, i.e., local time) per station for the whole of 2015. The RTPPP ZTDs were interpolated for each GPS station in turn, with the 40 other GPS station ZTD values providing the input. Hence, for ITD, per epoch, L_0 and β of equation (1) were estimated for the network and the turbulent component estimated per station. Validation was carried out by comparing the interpolated ZTDs with the RTPPP ZTD estimates themselves at 14:00 local time and computing the RMS difference and mean absolute error (MAE) for all stations for each day. This was repeated by using interpolation with the SKIm + Onn model.

The time series of the cross-validated daily MAE and RMS differences from the ITD and SKIm + Onn ZTD interpolation models are shown in Figure 3. It is clear that the ITD model leads to both lower annual mean MAE and RMS difference values than SKIm + Onn; i.e., the MAE and RMS reduce from 6.2 mm to 3.2 mm and 7.4 mm to 4.1 mm, respectively. It can also be seen from Figure 3 that the improvement of ITD is greater than that of SKIm + Onn in colder seasons (e.g., between days 0 to 100 and 280 to 365), when the medium-to-long wavelength turbulent signals are greater than the short wavelength ones and can be effectively modeled by ITD. This, in turn, enables stratified delays to be separated from the turbulent component in the ITD iterative process and better determined by using regression analysis. The performance of the two models is more similar in the summer (i.e., from around day of year 150 to 220), indicating that short wavelength water vapor effects are significant and variable and cannot be fully mitigated by either model.

Cross comparisons of the daily interpolated ZTD values are shown in Figure 4 for both the ITD and SKIm + Onn interpolation models, for all 41 stations for all of 2015. As for the time series, substantial reductions in the scatter are observed for ITD compared with those for SKIm + Onn; i.e., the RMS difference decreases

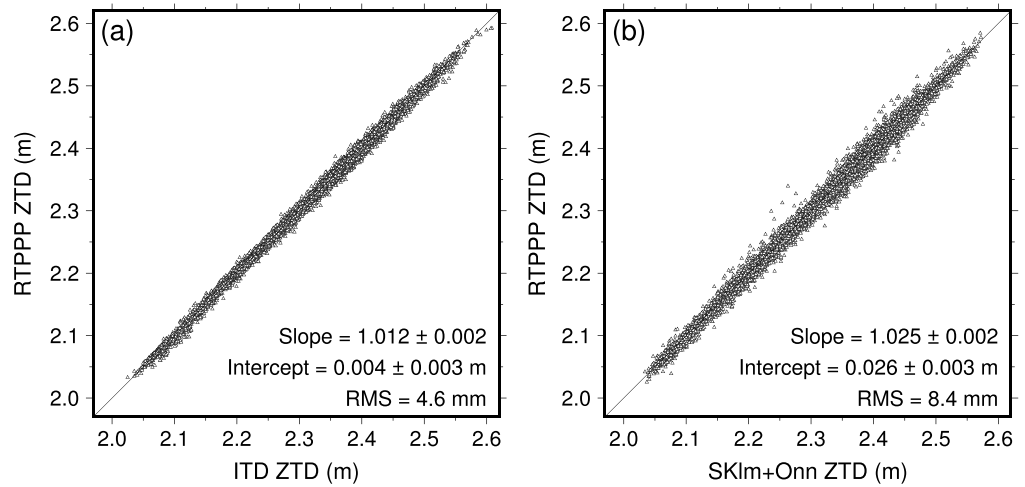


Figure 4. Cross validation of (a) ITD and (b) SKlm + Onn RTPPP ZTDs daily at 14:00 local time for 1 year for all the 41 GPS stations. Linear model (Initial RTPPP ZTD = Slope × Interpolated RTPPP ZTD + Intercept) was also applied.

from 8.4 mm to 4.6 mm. Small correlation and linear fit improvements are also obtained with ITD compared with SKlm + Onn: the correlation coefficient increases from 0.98 to 0.99, the linear fit improves from a slope of 1.025 to 1.012, and the intercept from 0.026 to 0.004 m, as detailed in Table 1. Furthermore, the proportion of differences under (magnitude) 10 mm increases from 61% for SKlm + Onn to 89% for ITD and increases from 32% to 69% for the proportion under 5 mm magnitude.

When considered for all stations for the entire year, the ITD interpolation model has been shown to substantially improve on the SKlm + Onn model. However, in the cross validation, some large differences occurred (more than 2 cm magnitude for both models), which suggests that the interpolation result is influenced by the GPS reference station distribution. To investigate this, the annual MAE and RMS differences per station are plotted in Figure 5, for both the ITD and SKlm + Onn models. It can be seen that the smaller MAE and RMS differences occur where the station coverage is denser, but the SKlm + Onn MAE and RMS values show substantial degradation compared with ITD in the northwest of the region where there are fewer stations, e.g., ~12 mm MAE for SKlm + Onn compared with ~5 mm for ITD. Meanwhile, the largest RMS value for any station is only ~8 mm for ITD, improved from ~12 mm for SKlm + Onn. Such station distribution degradations are consistent with the interpolation law and can be mitigated as far as possible by using stations with as uniform a distribution as possible. In terms of terrain effects on the MAE and RMS, for the ITD model, stations in the mountainous areas show approximately comparable precision with those at lower altitudes, whereas with SKlm + Onn, larger MAE and RMS values arise and the same applies in coastal areas. We attribute this improvement to the height scaling model working under the assumption that the turbulent delays are insignificant and have short wavelength compared with stratified delays; therefore, the height scaling is easily biased when strong tropospheric turbulence with medium-to-long wavelength signals occur.

Table 1. Summary of ITD and SKlm + Onn Model Interpolation Performance From Cross Validation of All ZTDs and All Common Epoch RTPPP and MODIS PWVs for All of 2015

χ^a	γ^a	No. of Data Points	Slope ^b	Intercept ^b	Correl. Coeff.	RMS (mm)
ITD ZTD	RTPPP ZTD	14,883	1.012 ± 0.002	0.004 ± 0.003 m	0.99	4.6
SKlm + Onn ZTD	RTPPP ZTD	14,883	1.025 ± 0.002	0.026 ± 0.003 m	0.98	8.4
ITD PWV	MODIS PWV ^c	8523	0.971 ± 0.002	0.329 ± 0.004 mm	0.98	1.48
SKlm + Onn PWV	MODIS PWV ^c	8523	0.948 ± 0.002	0.634 ± 0.004 mm	0.97	1.73
ITD map	MODIS map ^d	288 million	0.934 ± 0.003	1.223 ± 0.004 mm	0.97	1.71
SKlm + Onn map	MODIS map ^d	288 million	0.912 ± 0.002	2.101 ± 0.004 mm	0.96	1.96

^aThe linear model is $Y = \text{Slope} * X + \text{Intercept}$.

^bUncertainties are 95% confidence.

^cMODIS PWV pixels with co-located GPS stations.

^dAll available MODIS pixels.

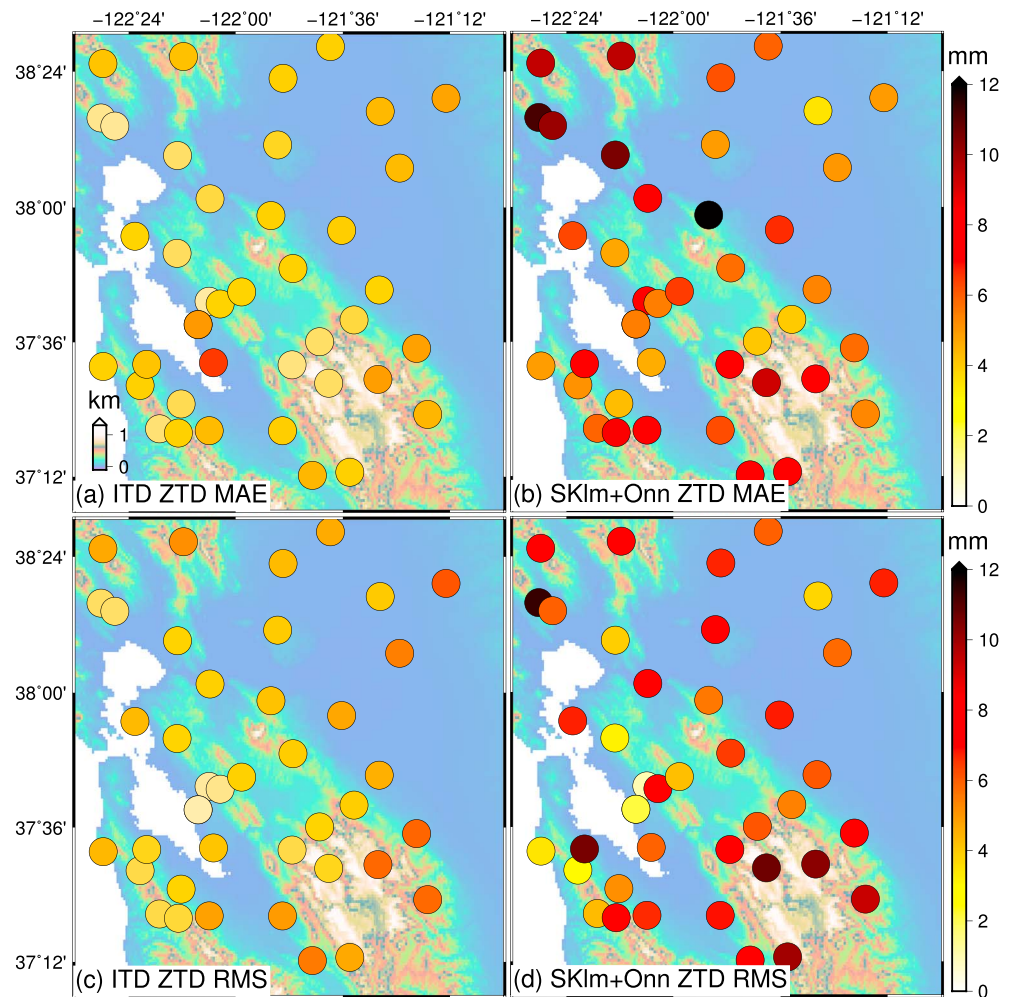


Figure 5. Spatial distribution of cross-validation ZTD results, showing the MAE and RMS of daily (14:00 local time) differences of interpolated versus RTPPP ZTDs, computed over all of 2015 per GPS station. (a) MAE using ITD, with an overall mean of 3.6 mm; (b) MAE using SKIm + Onn, with overall mean of 6.1 mm; (c) RMS using ITD, with an overall RMS of 4.6 mm; (d) RMS using SKIm + Onn, with an overall RMS of 8.4 mm.

5. Validation of Interpolated PWV Maps With MODIS

To provide further validation of the ITD interpolation model and its improvement over the SKIm + Onn model, including a detailed spatial resolution assessment, and to provide an accuracy assessment with an independent data set, the RTPPP GPS pointwise ZTD values were converted to PWV, interpolated to 1 km pixels across the entire study region, and compared with the MODIS near-IR PWV product. Pressure and temperature data at 5 min temporal resolution from co-located meteorological sensors were available at 4 of the 41 GPS stations and obtained from unavo.org. These were supplemented by 10 meteorological stations which were located up to 10 km outside the study region. The meteorological data were first interpolated to all 41 stations by using the *Li et al.* [2003] differential models, and according to their cross tests, the resulting pressure and temperature errors were less than 1 hPa and 2 K, respectively. The interpolated pressure measurements at each GPS station were used to directly compute ZHD by using the *Saastamoinen* [1972] model and subtracted from the RTPPP ZTD estimates, with the resulting ZWD pointwise values converted to PWV by using the *Bevis et al.* [1992] model with the interpolated surface temperature measurements. To enable the comparisons, 1 year MODIS Level 2 data from the Terra satellite were obtained across the study region, providing one PWV map at the Terra orbit track time of each day (during daytime, about 10:30 local time). The Level 2 data were generated at the 1 km spatial resolution of the MODIS instrument by using the near-IR algorithm [*Gao and Kaufman*, 2003]. About 30% of days had severe cloud conditions, so we excluded them as only a few grids

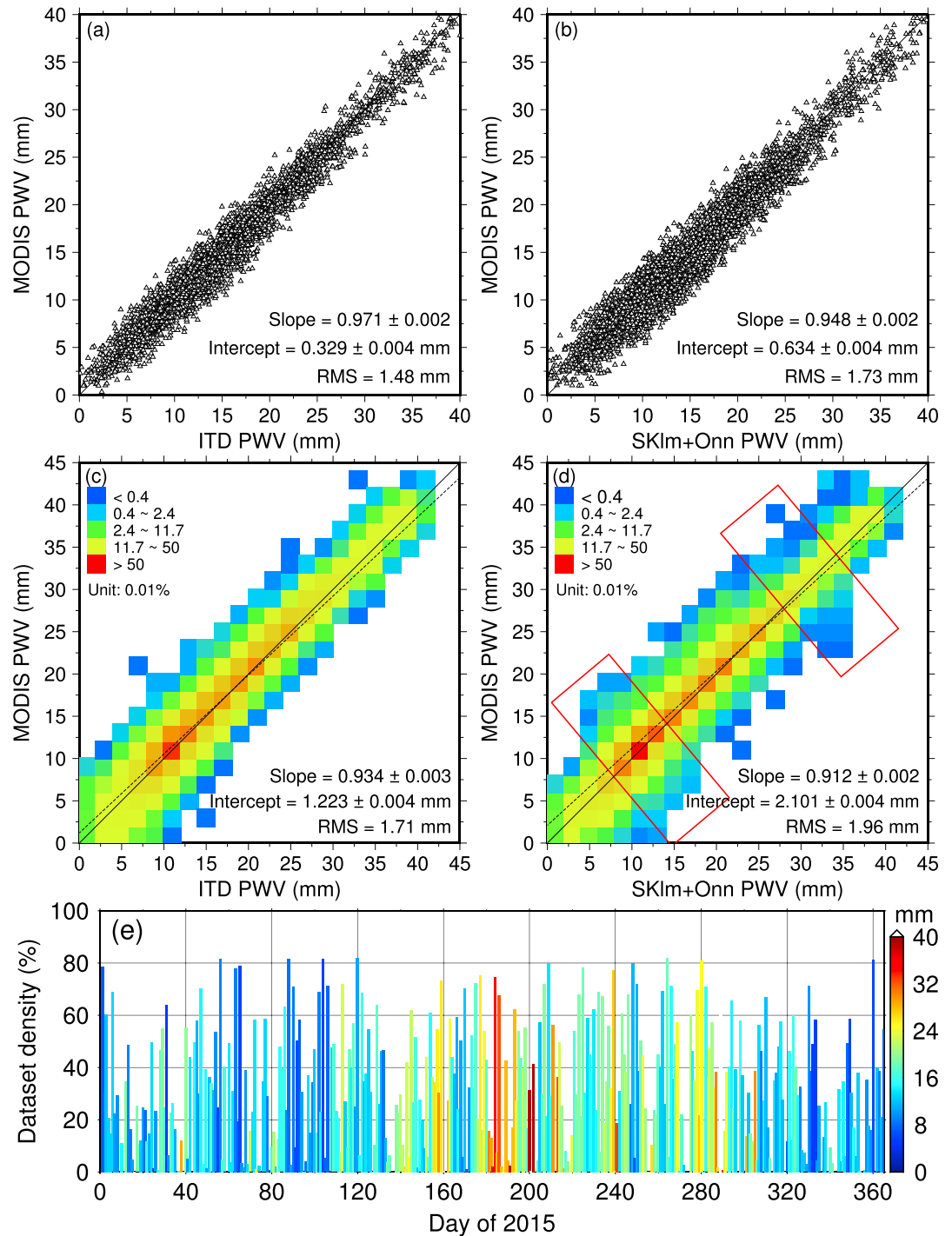


Figure 6. Cross validation of (a) ITD and (b) SKIm + Onn interpolated RTPPP GPS PWV with MODIS, using daily values at MODIS acquisition time on all 41 GPS stations for all of 2015. (c and d) All available pixels between MODIS PWV and ITD/SKIm + Onn PWV maps for year 2015. The color scale represents the density of occurrence, and the red boxes highlight instances of particular improvement (see section 5). (e) The daily cloud-free MODIS PWV pixel density is displayed, in which the vertical bar represents the total available pixel numbers divided by the maximum amount. The color scale represents the average daily PWV of all available pixels.

can be obtained. Areas with cloud conditions or above water were also masked, and only the cloud-free land areas were used in the comparison, with the percentage of data points available and used in the comparisons shown in Figure 6e, with the average cloud-free pixels over the entire year being 35%.

As the first step, cross validation was carried out at each GPS reference station, using one GPS PWV per day per station, taken at the MODIS acquisition time. We used MODIS PWV as “truth” values to validate the interpolated PWV at each GPS station (cross test), and the MODIS PWV values were averaged over boxes of 3×3 pixels centered on the GPS station’s location if the centered pixel was missing. While in such cases the spatial resolution of the MODIS PWV maps was effectively reduced from $1 \text{ km} \times 1 \text{ km}$ to $3 \text{ km} \times 3 \text{ km}$, this resolution is still much greater than the $\sim 15 \text{ km}$ GPS station spacing across the study region, providing a compromise between the resolution and maximizing the number of MODIS pixels for comparison. PWV cross comparisons for all daily values available for each GPS station for the whole of 2015 are shown in Figures 6a and 6b, with the RMS of the differences being 1.48 mm for the ITD model and 1.73 mm for SKIm + Onn, as also listed in Table 1. The ITD model also results in a better linear regression fit, with a slope of 0.97 and an intercept of 0.33 mm compared with respective values of 0.95 and 0.63 mm with the SKIm + Onn model, and the correlation coefficient increased from 0.97 to 0.98. The SKIm + Onn model also produced a greater mean difference than ITD during times of lower PWV content (i.e., 0–10 mm), with the more effective ITD modeling in the times with less water vapor (i.e., from midautumn to midspring) being consistent with the GPS cross-validation results shown in Figure 3, i.e., the improved separation of medium-to-long wavelength turbulence signals and improved performance across mountainous areas.

The interpolated RTPPP PWV values and resulting maps were then compared spatially with the MODIS PWV maps. The results are shown (RTPPP GPS minus MODIS) in Figure 7 for MODIS images acquired on 3 September and 19 November 2015, chosen as they are sample days which are virtually free from cloud conditions across the whole study region. The height for each grid cell was resampled by the 30 m Shuttle Radar Topography Mission DEM. Some large differences are visually apparent, mostly across the areas with frequent cloud masks and near San Francisco Bay, but MODIS PWVs above water areas also involve a different retrieval algorithm compared to those above the land, resulting in differences and discontinuities at the land edge. Furthermore, any values over water areas have been removed since PWVs above water (bay, lake, or ocean) share different characteristics from PWVs over land areas which cannot be well-described by the interpolation model [Sobrino *et al.*, 2003]. On average, the mountainous areas give more negative differences than flat terrain, showing that MODIS tends to overestimate PWV compared with GPS with increasing altitude (i.e., small PWV values), as previously found by Li *et al.* [2003]. It can also be seen in Figure 7 that the edge areas with fewer GPS stations produce larger differences than central areas, confirming as discussed in section 4 that improved GPS station coverage will improve the quality of interpolated PWV maps. The ITD model produces smoother difference maps than SKIm + Onn and has a lower percentage of large differences. ITD also performs much better than SKIm + Onn in coastal areas where the PWV is more changeable and gives more complicated turbulent components.

To further spatially assess the improvement of ITD RTPPP PWV values with MODIS over those from the SKIm + Onn model, differences between the RTPPP interpolated PWV and all MODIS pixels (cloud free) were computed across the study region bounded by the GPS stations for the entire year 2015 and for all weather conditions. The differences are shown in Figures 6c and 6d, for each of the ITD and SKIm + Onn models. In general, most PWV pairs are located along the 1:1 line, implying a strong correlation between the RTPPP-based PWV and MODIS PWV maps. The SKIm + Onn PWV plot exhibits greater differences in comparison with the ITD PWV plot. The scatters are distributed rather unsymmetrically, especially when the PWV amounts fell between 5–15 mm (typically for mountainous areas) and 30–35 mm due to the lower scale factor (0.912 versus 0.934).

To illustrate the finer spatial detail of PWV and the performance of interpolated RTPPP PWV, in Figure 8 we plot ITD-based PWVs over mountainous areas, shown as $37^{\circ}09'$ to $38^{\circ}30'$ in latitude and $-122^{\circ}12'$ to $-121^{\circ}00'$ in longitude (Figure 8a) and $37^{\circ}09'$ to $37^{\circ}50'$ in latitude and $-122^{\circ}30'$ to $-121^{\circ}00'$ in longitude (Figure 8b), for 3 September 2015. In Figure 8 we include PWV profiles (smoothed by using a tenth averaging window) for both ITD RTPPP and MODIS along lines of constant latitude and longitude, over both mountainous and flat areas, which enable detailed comparisons of the ITD PWV gradients with respect to topography. The ITD PWV profiles change in a similar tendency with MODIS and share similar gradients. The overall RMS

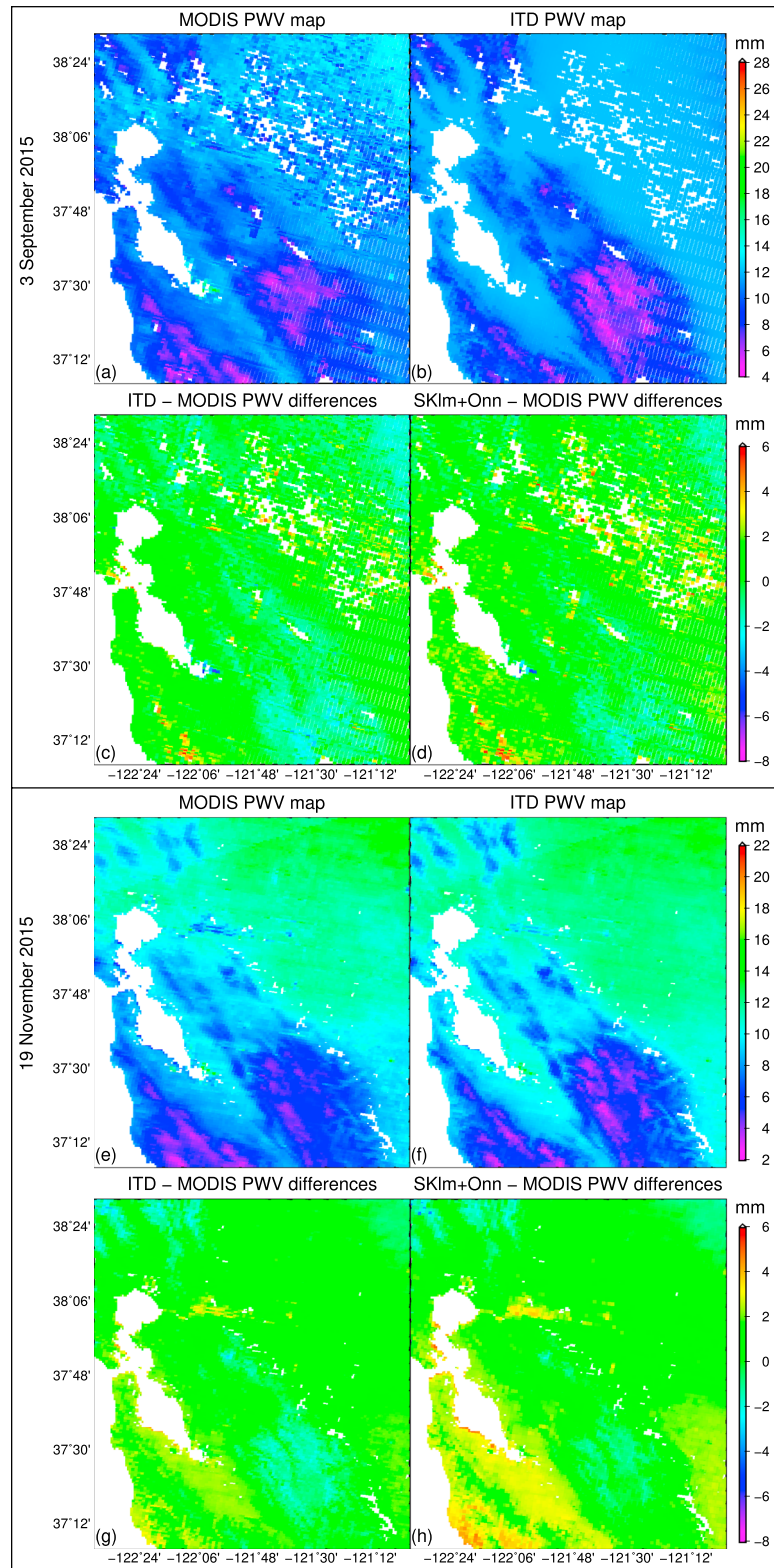


Figure 7. MODIS PWV and ITD RTPPP GPS PWV maps and RTPPP GPS minus MODIS PWV difference maps at 1 km spatial resolution, for both ITD and SKIm + Onn interpolations. (a–d) 3 September 2015 and (e–h) 19 November 2015. MODIS maps (Figures 7a and 7e), ITD maps (Figures 7b and 7f), ITD difference maps (Figures 7c and 7g), and SKIm + Onn difference maps (Figures 7d and 7h). The large differences (red pixels) in the northeast of Figures 7c and 7d are likely due to the presence of thin clouds which are not labeled in the cloud mask product.

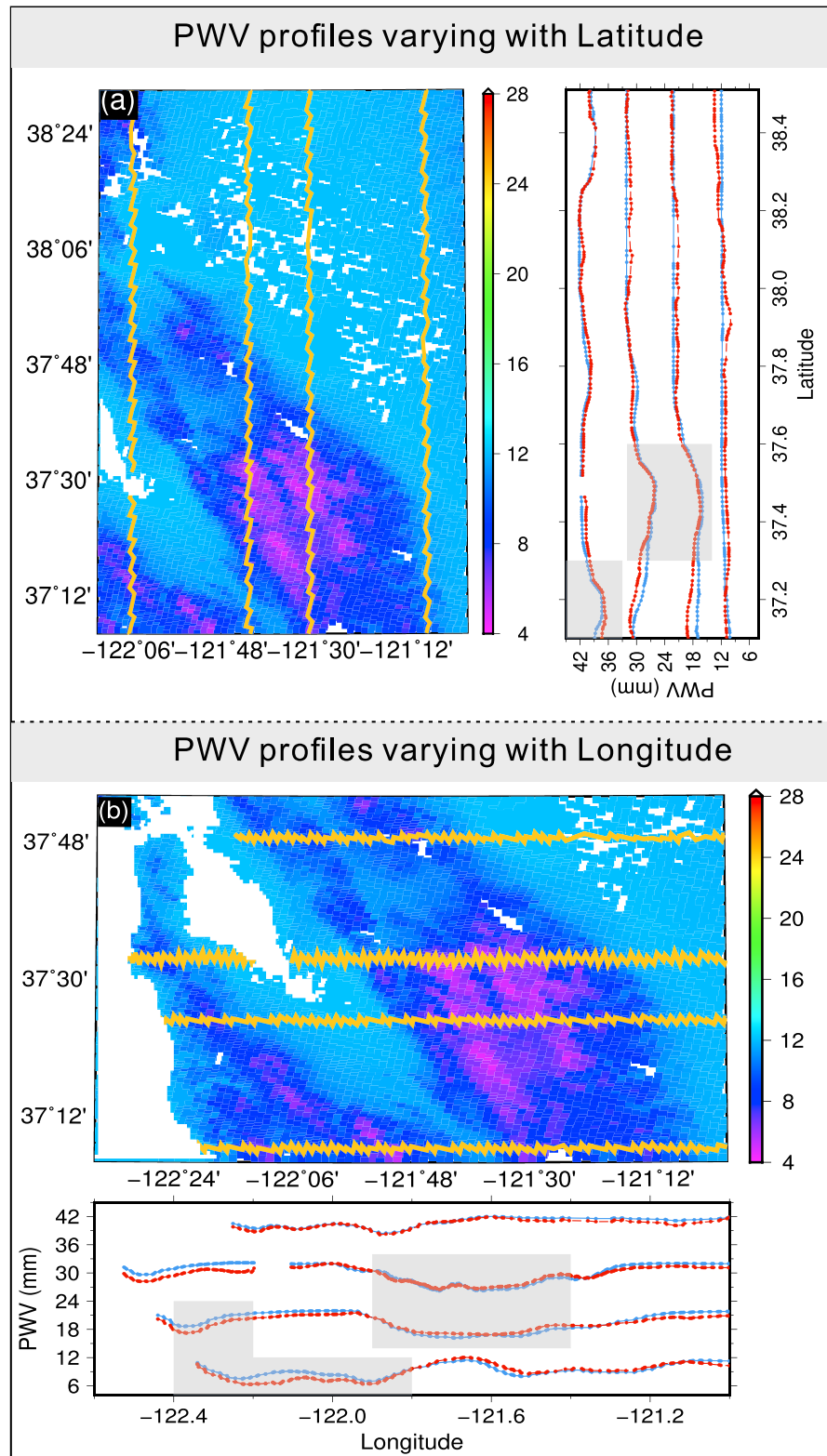


Figure 8. ITD RTPPP map and MODIS PWV (red line) and ITD RTPPP PWV (blue line) profiles along certain (a) latitudes and (b) longitudes, after shifting a constant number, for 3 September 2015. The PWV profile series are in the same order as the line segments in the PWV map and are averaged by a tenth average window. The gray polygon areas represent the mountain area. The overall RMS difference between MODIS and ITD PWV along the eight profiles is 1.51 mm, and the RMS differences for the mountainous (gray polygon) and flat areas are 1.57 mm and 1.47 mm, respectively.

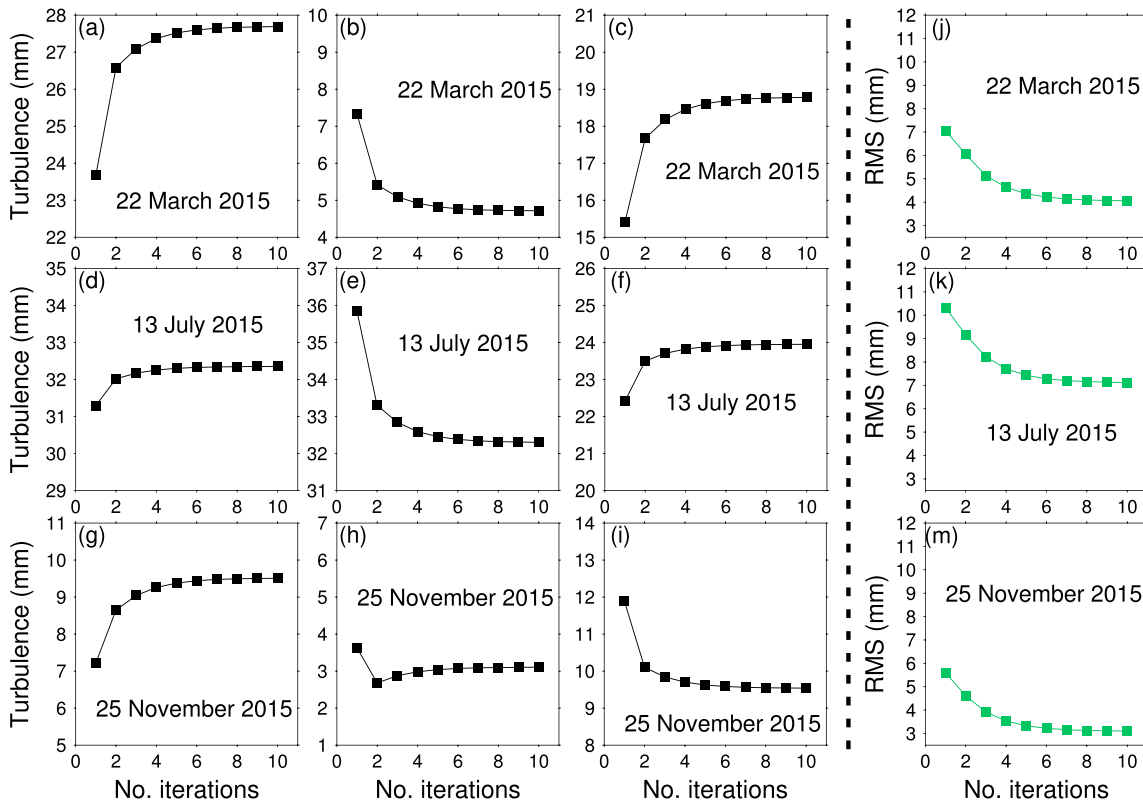


Figure 9. RTPPP ZTD turbulent components separated by ITD at each iteration step. Stations (first column) P177, (second column) P230, and (third column) S300. (fourth column) ZTD cross-validation RMS difference for all 41 stations on the corresponding day. Shown for sample days in each of spring, summer, and autumn.

difference between MODIS and ITD PWV for the eight profiles considered is 1.51 mm, and the RMS differences for mountain (gray polygon in Figure 8) and flat areas are 1.57 mm and 1.47 mm, respectively. These agreements demonstrate that the ITD model is capable of retrieving detailed water vapor distributions over a wide region, thereby showing its potential application for monitoring local extreme weather events.

6. Discussion on Tropospheric Turbulence

The principal aim of the ITD model is to separate the elevation-dependent ZTD/PWV component from the turbulent component, which is the most variable and uncertain part, and can easily bias the vertical ZTD scaling, making the separation of the two components challenging. Due to the constraints of the density of GPS stations, only medium-to-long wavelength turbulent signals are expected to be successfully modeled by using ITD. To illustrate the size and variation of the turbulent component, and the importance of iterating the solution until convergence arises, a sample with three GPS stations was considered: P177, P230, and S300 (Figure 1), which are in different parts of the study region, are at different elevations, and are at varying distances from the nearest other GPS reference stations. P177 is near the ocean, while S300 and P230 are in mountainous areas with elevations of ~500 m and ~700 m, respectively. Three epochs from different seasons (spring, summer, and autumn) were considered, and the variation of the turbulent component and its convergence with the number of iterations is illustrated in Figure 9.

It is clear from Figure 9 that the turbulent ZTD component can reach several centimeters and can be efficiently separated from the elevation-dependent component. Although the first iteration enables the majority of the turbulent component to be determined, the subsequent iterations are needed for robust estimation. Figure 9 (fourth column) further indicates the performance improvement with increasing number of iterations, with the RMS difference (computed through the RTPPP ZTD cross validation from all 41 stations at the corresponding epoch of each row) becoming smaller and tending toward convergence. Around six iterations are typically needed for convergence, after which submillimeter RMS changes arise, with improvements of typically less than 1 mm.

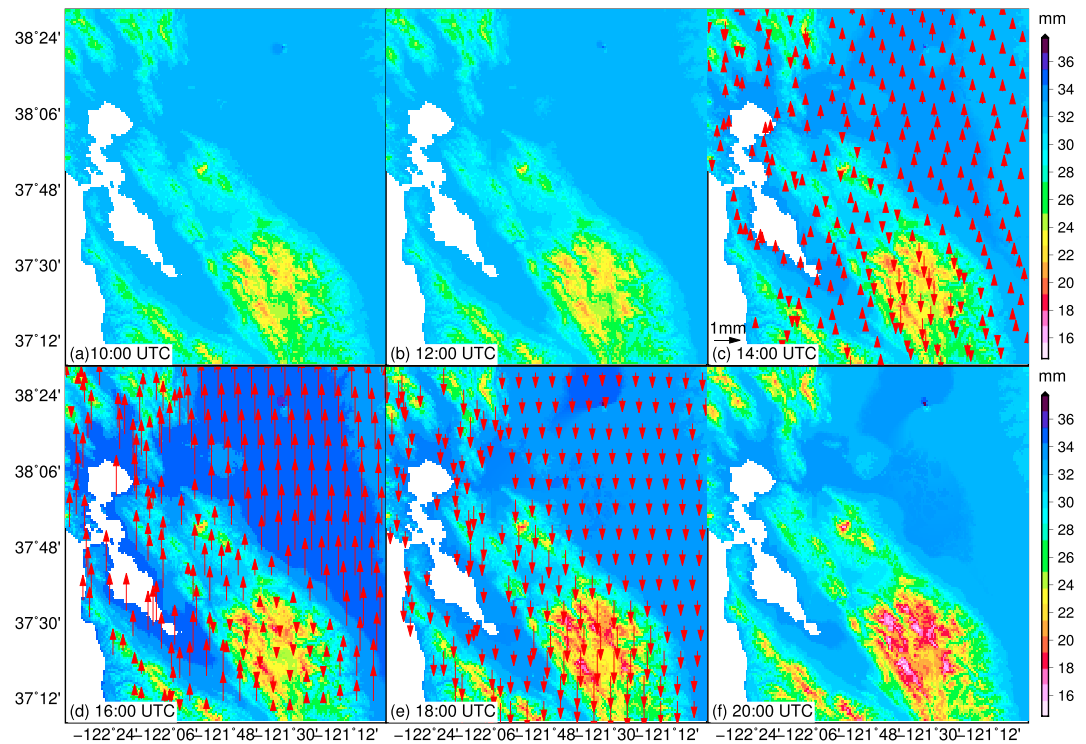


Figure 10. RTPPP PWV fields across the California study region every 2 h on 2 November 2015 during a rainfall process (a–f) from 10:00 to 20:00 UTC. The arrows represent PWV increasing (upward) or decreasing (downward) during the preceding 2 h.

As the most important feature of the ITD model, the convergence tendency in Figure 9 reveals that the turbulence effect can be reduced by separating the stratified and turbulent components through iteration. The decoupling procedure acts very similarly to robust estimation, in which the ZTDs from stations exhibiting strong turbulence will contribute less in height scaling but account for more in the turbulent delay interpolation. In this way, the systematic patterns of turbulence resulting from local weather conditions or topography [Betts, 2001; Cho *et al.*, 2003] can be modeled better. The iteration also allows for the detection of ZTD outliers, which is a not uncommon occurrence in real-time PPP due to the unpredictable behavior of the satellite clocks. Consequently, the ITD model enables both fitting of the tropospheric vertical profiles and modeling of the turbulence processes. As the fourth column in Figure 9 suggests, successfully accounting for this results in the overall RMS difference of the cross validation test reducing and converging.

7. Conclusions and Outlook

In this study, an iterative tropospheric decomposition model has been developed for the generation of high-resolution regional tropospheric PWV fields (maps) from the interpolation of pointwise GPS ZTDs, without any data differencing. For a California study region of around 150 km × 150 km, the approach of decoupling the terrain elevation dependency and the tropospheric turbulence contribution to ZTD in an iterative procedure (typically 4–6 iterations were required) led to improved accuracy interpolated tropospheric water vapor maps over those based on previous studies, such as the tropospheric turbulence and elevation-dependent model SKIm + Onn of Xu *et al.* [2011]. To not only be applicable to postprocessed SAR atmospheric corrections but also facilitate SAR for rapid response to monitoring earthquakes and volcanoes, Network RTK positioning, and meteorological forecasting, we used real-time mode PPP GPS ZTD values estimated every 5 min (which were validated with postprocessed GIPSY ZTDs with an overall RMS difference of 12.5 mm for all 41 stations for all of 2015) to generate the tropospheric maps. Cross validation of the GPS ZTD values resulted in 4.6 mm RMS differences by using the ITD model compared with 8.4 mm by using the SKIm + Onn model, using one value per station per day (14:00 local time) for all of 2015. Whereas the SKIm + Onn interpolation model has degraded performance over mountainous areas, the cross-validation ITD model RMS and mean

differences are similar for both mountainous and flatter terrain and also similar for both coastal and inland areas. The cross-validation improvements using ITD are smallest in the summer months. Spatially, we generated PWV values for 1 km pixels for all land-covered parts of the region and compared with daily MODIS PWV near-IR product values, with the RMS difference for the year being improved from 1.96 mm by using the SKIm + Onn model to 1.71 mm by using ITD. Furthermore, the spatial PWV gradients using the ITD model and MODIS across a variety of topography were nearly identical to each other. The overall RMS difference between MODIS and ITD PWV profiles is 1.51 mm, and the RMS differences for mountain and flat areas are 1.57 mm and 1.47 mm, respectively. Hence, the ITD PWV fields are also able to reveal detailed water vapor information over varying terrains.

To provide an indication of the potential of the real-time mode ITD model interpolated tropospheric maps for meteorological and geodetic applications, including revealing detailed information of local weather processes, we show in Figure 10 the detailed 2-hourly PWV information during a rainfall process over the study region on 2 November 2015 (10 A.M. to 8 P.M. UTC). The arrows represent the PWV increasing (upward) or decreasing (downward) during each preceding 2 h. One important fact is that the PWV over mountainous areas decreased during the whole rainfall process, but other areas experienced increasing and decreasing PWV before and after the rainfall, respectively. We do not explain the patterns further as the focus of this paper is on showing the quality of RTPPP ZTD and PWV maps.

The generated spatially dense PWV fields with continuous, high (5 min) temporal resolution are not only suitable for correcting atmospheric effects in SAR images at the instant of acquisition but will also ensure the identification of water vapor variation from ground motion between image acquisition times [Foster *et al.*, 2006]. What is more, the high performance of the dense PWV maps using the ITD model is especially useful for mitigating the effects of water vapor for SAR measurements in mountainous areas, which usually suffer from vertical stratification and turbulent mixing due to the orography [Wadge *et al.*, 2002].

In the near future, more research is planned to investigate the capacity of high-resolution real-time tropospheric products using the ITD interpolation model. This includes the testing of the ITD model on ECMWF ZTD, MODIS, and radiosonde PWV in addition to the GPS interpolations considered here. The abundant data sources will contribute to generate global coverage and all weather condition dense water vapor fields and to further investigate detailed tropospheric turbulence characteristics and processes.

Acknowledgments

The GPS data sets and orbit/clock products used in this paper were gratefully obtained from the PBO (<http://pbo.unavco.org/data/gps>) and the IGS Real-time Service, respectively. We also acknowledge UNAVCO for the operation of the PBO and for providing high-accuracy station coordinate time series and tropospheric products, along with Central Washington University. The authors also thank NASA for MODIS water vapor data. This work was supported by a Chinese Scholarship Council studentship awarded to Chen Yu. Part of this work was also supported by the UK Natural Environmental Research Council (NERC) through the Centre for the Observation and Modelling of Earthquakes, Volcanoes and Tectonics (COMET, ref.: come30001) and the LICs and CEDRRIC projects (refs. NE/K010794/1 and NE/N012151/1, respectively) and the ESA-MOST DRAGON-4 projects (ref. 32244). The figures were generated using the Generic Mapping Tools software [Wessel *et al.*, 2013].

References

- Ahmed, F., P. Vlacovic, F. N. Teferle, J. Douša, R. Bingley, and D. Laurichesse (2016), Comparative analysis of real-time precise point positioning zenith total delay estimates, *GPS Solut.*, *20*(2), 187–199.
- Albert, P., R. Bennartz, and J. Fischer (2001), Remote sensing of atmospheric water vapor from backscattered sunlight in cloudy atmospheres, *J. Atmos. Oceanic Technol.*, *18*, 865–874.
- Aumann, H. H., et al. (2003), AIRS/AMSU/HSB on the Aqua mission: Design, science objectives, data products, and processing systems, *IEEE T. Geosci. Remote.*, *41*, 253–264.
- Bekaert, D. P. S., A. Hooper, and T. J. Wright (2015), A spatially variable power law tropospheric correction technique for InSAR data, *J. Geophys. Res. Solid Earth*, *120*, 1345–1356, doi:10.1002/2014JB011558.
- Benevides, P., J. Catalao, and P. M. A. Miranda (2015), On the inclusion of GPS precipitable water vapour in the nowcasting of rainfall, *Nat. Hazards Earth Syst. Sci.*, *15*, 2605–2616.
- Benevides, P., G. Nico, J. Catalao, and P. M. A. Miranda (2016), Bridging InSAR and GPS tomography: A new differential geometrical constraint, *IEEE T. Geosci. Remote.*, *54*(2), 697–702.
- Bennartz, R., and J. Fischer (2001), Retrieval of columnar water vapour over land from back-scattered solar radiation using the Medium Resolution Imaging Spectrometer (MERIS), *Remote Sens. Environ.*, *78*, 271–280.
- Bennett, G. V., and A. Jupp (2012), Operational assimilation of GPS zenith total delay observations into the Met Office numerical weather prediction models, *Mon. Weather Rev.*, *140*, 2706–2719.
- Berrada Baby, H., P. Gole, and J. Lavergnat (1988), A model for the tropospheric excess path length of radio waves from surface meteorological measurements, *Radio Sci.*, *23*(6), 1023–1038, doi:10.1029/RS023i006p01023.
- Betts, R. A. (2001), Biogeophysical impacts of land use on present-day climate: Near-surface temperature change and radiative forcing, *Atmos. Sci. Lett.*, *2*(1–4), 39–51.
- Bevis, M., S. Businger, T. Herring, C. Rocken, R. Anthes, and R. Ware (1992), GPS meteorology: Remote sensing of atmospheric water vapor using the Global Positioning System, *J. Geophys. Res.*, *97*(D14), 15,787–15,801, doi:10.1029/92JD01517.
- Beyerle, G. (2009), Carrier phase wind-up in GPS reflectometry, *GPS Solut.*, *13*(3), 191–198.
- Boehm, J., A. Niell, P. Tregoning, and H. Schuh (2006a), Global Mapping Function (GMF): A new empirical mapping function based on numerical weather model data, *Geophys. Res. Lett.*, *33*, L07304, doi:10.1029/2005GL025546.
- Boehm, J., B. Werl, and H. Schuh (2006b), Troposphere mapping functions for GPS and very long baseline interferometry from European Centre for Medium-Range Weather Forecasts operational analysis data, *J. Geophys. Res.*, *111*, B02406, doi:10.1029/2005JB003629.
- Boniface, K., V. Ducrocq, G. Jaubert, X. Yan, P. Brousseau, F. Masson, C. Champollion, J. Ch'ery, and E. Doerflinger (2009), Impact of high-resolution data assimilation of GPS zenith delay on Mediterranean heavy rainfall forecasting, *Ann. Geophys.*, *27*, 2739–2753.

- Brasington, J., J. Langham, and B. Rumsby (2003), Methodological sensitivity of morphometric estimates of coarse fluvial sediment transport, *Geomorphology*, *53*, 299–316.
- Cho, J. Y. N., R. E. Newell, B. E. Anderson, J. D. W. Barrick, and K. L. Thornhill (2003), Characterizations of tropospheric turbulence and stability layers from aircraft observations, *J. Geophys. Res.*, *108*(D20), 8784, doi:10.1029/2002JD002820.
- De Paoli, L., and G. E. Flowers (2009), Dynamics of a small surge-type glacier using one-dimensional geophysical inversion, *J. Glaciol.*, *55*(194), 1101–1112.
- Divakarla, M. G., C. D. Barnett, M. D. Goldberg, L. M. McMillin, E. Maddy, W. Wolf, L. Zhou, and X. Liu (2006), Validation of Atmospheric Infrared Sounder temperature and water vapor retrievals with matched radiosonde measurements and forecasts, *J. Geophys. Res.*, *111*, D09515, doi:10.1029/2005JD006116.
- Elliott, J. R., J. Biggs, B. Parsons, and T. J. Wright (2008), InSAR slip rate determination on the Altyn Tagh Fault, northern Tibet, in the presence of topographically correlated atmospheric delays, *Geophys. Res. Lett.*, *35*, L12309, doi:10.1029/2008GL036659.
- Emardson, T. R., and J. M. Johansson (1998), Spatial interpolation of the atmospheric water vapor content between sites in a ground-based GPS network, *Geophys. Res. Lett.*, *25*(17), 3347–3350, doi:10.1029/98GL02504.
- Fattahi, H., and F. Amelung (2015), InSAR bias and uncertainty due to the systematic and stochastic tropospheric delay, *J. Geophys. Res. Solid Earth*, *120*, 8758–8773, doi:10.1002/2015JB012419.
- Fialko, Y. (2006), Interseismic strain accumulation and the earthquake potential on the southern San Andreas fault system, *Nature*, *441*, 968–971, doi:10.1038/nature04797.
- Foster, J., B. Brooks, T. Cherubini, C. Shacat, S. Businger, and C. L. Werner (2006), Mitigating atmospheric noise for InSAR using a high resolution weather model, *Geophys. Res. Lett.*, *33*, L16304, doi:10.1029/2006GL026781.
- Gao, B. C., and Y. J. Kaufman (2003), Water vapor retrievals using Moderate Resolution Imaging Spectroradiometer (MODIS) near-infrared channels, *J. Geophys. Res.*, *108*(D13), 4389, doi:10.1029/2002JD003023.
- Gelb, A. (1974), *Applied Optimal Estimation*, MIT Press, Cambridge, Mass.
- Genrich, J. F., and Y. Bock (2006), Instantaneous geodetic positioning with 10–50 Hz GPS measurements: Noise characteristics and implications for monitoring networks, *J. Geophys. Res.*, *111*, B03403, doi:10.1029/2005JB003617.
- Gilli, J. A., J. Corominas, and J. Rius (2000), Using Global Positioning System techniques in landslide monitoring, *Eng. Geol.*, *55*(3), 167–192.
- Gourmelen, N., and F. Amelung (2005), Postseismic mantle relaxation in the Central Nevada Seismic Belt, *Science*, *310*, 1473–1476, doi:10.1126/science.1119798.
- Gundlich, B., and K. R. Koch (2002), Confidence regions for GPS baselines by Bayesian statistics, *J. Geod.*, *76*(1), 55–62.
- Im, S., S. Hurllebaus, and Y. Kang (2013), Summary review of GPS technology for structural health monitoring, *J. Struct. Eng.*, *139*(10), 1653–1664.
- Janssen, V., L. Ge, and C. Rizo (2004), Tropospheric corrections to SAR interferometry from GPS observations, *GPS Solut.*, *8*, 140–151.
- Jarlemark, P. O., and T. R. Emardson (1998), Strategies for spatial and temporal extrapolation and interpolation of wet delay, *J. Geod.*, *72*(6), 350–355.
- Jolivet, R., P. S. Agram, N. Y. Lin, M. Simons, M.-P. Doin, G. Peltzer, and Z. Li (2014), Improving InSAR geodesy using Global Atmospheric Models, *J. Geophys. Res. Solid Earth*, *119*, 2324–2341, doi:10.1002/2013JB010588.
- Kouba, J. (2009), A guide to using International GNSS Service (IGS) products. [Available at <http://igsceb.jpl.nasa.gov/igsceb/resource/pubs/UsingGPSProductsVer21.pdf>].
- Leandro, R., M. C. Santos, and R. B. Langley (2006), UNB neutral atmosphere models: Development and performance, *Proc. ION NTM*, *52*(1), 564–573.
- Lee, J.-M., J.-Y. Park, and J.-Y. Choi (2013), Evaluation of sub-aerial topographic surveying techniques using total station and RTK-GPS for applications in macrotidal sand beach environment, *J. Coastal Res.*, *65*, 535–540.
- Li, X., G. Dick, M. Ge, S. Heise, J. Wickert, and M. Bender (2014), Real-time GPS sensing of atmospheric water vapor: Precise point positioning with orbit, clock, and phase delay corrections, *Geophys. Res. Lett.*, *41*, 3615–3621, doi:10.1002/2013GL058721.
- Li, Z., J. P. Muller, and P. Cross (2003), Comparison of precipitable water vapor derived from radiosonde, GPS, and Moderate-Resolution Imaging Spectroradiometer measurements, *J. Geophys. Res.*, *108*(D20), 4651, doi:10.1029/2003JD003372.
- Li, Z., J. P. Muller, P. Cross, and E. J. Fielding (2005), Interferometric synthetic aperture radar (InSAR) atmospheric correction: GPS, Moderate Resolution Imaging Spectroradiometer (MODIS), and InSAR integration, *J. Geophys. Res.*, *110*, B03410, doi:10.1029/2004JB003446.
- Li, Z., E. J. Fielding, P. Cross, and J.-P. Muller (2006a), Interferometric synthetic aperture radar atmospheric correction: GPS topography-dependent turbulence model, *J. Geophys. Res.*, *111*, B02404, doi:10.1029/2005JB003711.
- Li, Z., E. J. Fielding, P. Cross, and J.-P. Muller (2006b), Interferometric synthetic aperture radar atmospheric correction: Medium Resolution Imaging Spectrometer and Advanced Synthetic Aperture Radar integration, *Geophys. Res. Lett.*, *33*, L06816, doi:10.1029/2005GL025299.
- Li, Z., J.-P. Muller, P. Cross, P. Albert, J. Fischer, and R. Bennartz (2006c), Assessment of the potential of MERIS near-infrared water vapour products to correct ASAR interferometric measurements, *Int. J. Remote Sens.*, *27*, 349–365, doi:10.1080/01431160500307342.
- Li, Z., E. J. Fielding, and P. Cross (2009a), Integration of InSAR time series analysis and water vapour correction for mapping postseismic deformation after the 2003 Bam, Iran earthquake, *IEEE T. Geosci. Remote.*, *47*, 3220–3230.
- Li, Z., E. J. Fielding, P. Cross, and R. Preusker (2009b), Advanced InSAR atmospheric correction: MERIS/MODIS combination and stacked water vapour models, *Int. J. Remote Sens.*, *30*, 3343–3363.
- Liou, Y. A., Y. T. Teng, T. Van Hove, and J. C. Liljegren (2001), Comparison of precipitable water observations in the near tropics by GPS, microwave radiometer, and radiosondes, *J. Appl. Meteorol.*, *40*(1), 5–15.
- McCarthy, D. D. (1996), IERS conventions (1996) IERS Technical Note 21. US Naval Observatory.
- Mengistu Tsidu, G., T. Blumenstock, and F. Hase (2015), Observations of precipitable water vapour over complex topography of Ethiopia from ground-based GPS, FTIR, radiosonde and ERA-Interim reanalysis, *Atmos. Meas. Tech.*, *8*, 3277–3295.
- Ohtani, R., and I. Naito (2000), Comparisons of GPS-derived precipitable water vapors with radiosonde observations in Japan, *J. Geophys. Res.*, *105*(D22), 26,917–26,929, doi:10.1029/2000JD900362.
- Onn, F., and H. A. Zebker (2006), Correction for interferometric synthetic aperture radar atmospheric phase artifacts using time series of zenith wet delay observations from a GPS network, *J. Geophys. Res.*, *111*, B09102, doi:10.1029/2005JB004012.
- Pérez-Ruiz, M., J. Carballido, J. Agüera, and J. A. Gil (2011), Assessing GNSS correction signals for assisted guidance systems in agricultural vehicles, *Precis. Agric.*, *12*(5), 639–652.
- Poli, P., P. Moll, F. Rabier, G. Desroziers, B. Chapnik, L. Berre, S. B. Healy, E. Andersson, and F.-Z. El Guelai (2007), Forecast impact studies of zenith total delay data from European near real-time GPS stations in Météo France 4DVAR, *J. Geophys. Res.*, *112*, D06114, doi:10.1029/2006JD007430.

- Raja, M. K. R. V., S. I. Gutman, J. G. Yoe, L. M. McMillin, and J. Zhao (2008), The validation of AIRS retrievals of integrated precipitable water vapor using measurements from a network of ground-based GPS receivers over the contiguous United States, *J. Atmos. Oceanic Technol.*, *25*, 416–428.
- Saastamoinen, J. (1972), Atmospheric correction for the troposphere and stratosphere in radio ranging of satellites, in *The Use of Artificial Satellites for Geodesy, Geophys. Monogr.*, vol. 15, pp. 247–251, AGU, Washington, D. C.
- Shoji, Y., M. Kunii, and K. Saito (2011), Mesoscale data assimilation of Myanmar cyclone Nargis Part II: Assimilation of GPS-derived precipitable water vapor, *J. Meteorol. Soc. Jpn.*, *89*(1), 67–88.
- Sobrino, J. A., J. El Kharraz, and Z. L. Li (2003), Surface temperature and water vapour retrieval from MODIS data, *Int. J. Remote Sens.*, *24*(24), 5161–5182.
- Treuhaf, R. N., and G. E. Lanyi (1987), The effect of the dynamic wet troposphere on radio interferometric measurements, *Radio Sci.*, *22*(2), 251–265, doi:10.1029/RS022i002p00251.
- Wadge, G., et al. (2002), Atmospheric models, GPS and InSAR measurements of the tropospheric water vapour field over Mount Etna, *Geophys. Res. Lett.*, *29*(19), 1905, doi:10.1029/2002GL015159.
- Walters, R. J., J. R. Elliott, Z. Li, and B. Parsons (2013), Rapid strain accumulation on the Ashkabad fault (Turkmenistan) from atmosphere-corrected InSAR, *J. Geophys. Res. Solid Earth*, *118*, 3674–3690.
- Wen, Y., Z. Li, C. Xu, I. Ryder, and R. Bürgmann (2012), Postseismic motion after the 2001 M_w 7.8 Kokoxili earthquake in Tibet observed by InSAR time series, *J. Geophys. Res.*, *117*, B08405, doi:10.1029/2011JB009043.
- Wessel, P., W. H. F. Smith, R. Scharroo, J. Luis, and F. Wobbe (2013), Generic Mapping Tools: Improved version released, *Eos Trans. AGU*, *94*(45), 409–410, doi:10.1002/2013EO450001.
- Williams, S., Y. Bock, and P. Fang (1998), Integrated satellite interferometry: Tropospheric noise, GPS estimates and implications for interferometric synthetic aperture radar products, *J. Geophys. Res.*, *103*(B11), 27,051–27,067, doi:10.1029/98JB02794.
- Wright, T. J., B. Parsons, P. C. England, and E. J. Fielding (2004), InSAR observations of low slip rates on the major faults of western Tibet, *Science*, *305*, 236–239.
- Xu, W. B., Z. W. Li, X. L. Ding, and J. J. Zhu (2011), Interpolating atmospheric water vapor delay by incorporating terrain elevation information, *J. Geod.*, *85*(9), 555–564.
- Yan, X., V. Ducrocq, G. Jaubert, P. Brousseau, P. Poli, C. Champollion, C. Flamant, and K. Boniface (2009), The benefit of GPS zenith delay assimilation to high-resolution quantitative precipitation forecasts: A case-study from COPS IOP 9, *Q. J. R. Meteorol. Soc.*, *135*(644), 1788–1800.
- Yao, Y., C. Yu, and Y. Hu (2014), A new method to accelerate PPP convergence time by using a global zenith troposphere delay estimate model, *J. Navig.*, *67*(5), 899–910.
- Zabuski, L., W. Świdziński, M. Kulczykowski, T. Mrozek, and I. Laskowicz (2015), Monitoring of landslides in the Brda river valley in Koronowo (Polish Lowlands), *Environ. Earth Sci.*, *73*(12), 8609–8619.
- Zumberge, J. F., M. B. Heflin, D. C. Jefferson, M. M. Watkins, and F. H. Webb (1997), Precise point positioning for the efficient and robust analysis of GPS data from large networks, *J. Geophys. Res.*, *102*, 5005–5017, doi:10.1029/96JB03860.